ACS Partner Journal

ACCOUNTS of materials research

pubs.acs.org/amrcda

Article

4D Synchrotron X-ray Nanoimaging for Early Age Cement Curing: Where Are We and Where Should We Go?

Miguel A.G. Aranda*

Cite This: *Acc. Mater. Res.* 2025, 6, 814−827

Read Online

ACCESS | Metrics & More | Article Recommendations

CONSPECTUS: The production of cement is a key indicator of a region's level of development. As such, its use is essential for any society aiming to create healthy, comfortable, safe and secure living and working environments. However, these benefits come at a price; Portland cement production accounts for ≈8% of the total anthropogenic CO_2 emissions. If cement fabrication was considered a country, it would rank as the third largest emitter, after China and the United States. Consequently, reducing the CO_2 footprint of the construction industry is a societal need. Numerous low-carbon cement alternatives have been proposed, primarily involving the partial substitution of Portland clinker with materials that possess much lower CO_2 footprints. However, these cements have not been widely adopted because they exhibit reduced mechanical strength at 1 day of hydration, failing to meet current practices for formwork stripping. Therefore, a primary objective is to elucidate the mechanisms of early age cement hydration to accelerate their hydration rates.

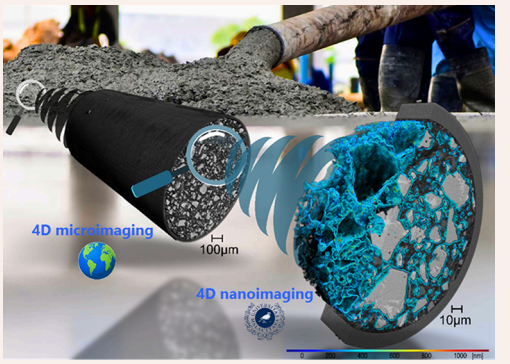

Portland cement and low-carbon cements are complex, multimineral materials comprising at least seven crystalline components. Additionally, during the hydration process, new hydrate phases − both crystalline and amorphous − are formed, resulting in the development of intricate, time-dependent microstructures. The compositional and spatial complexity, along with the inherent heterogeneity, underscores the necessity for additional analytical tools such as 3D synchrotron X-ray imaging techniques. Furthermore, as dissolution and precipitation processes are time-dependent, advanced 4D (3D + time) imaging tools are essential. Many pertinent features, such as alite etch-pits, alite reaction zone, and calcium silicate hydrate (C−S−H) gel shells and needles, are submicrometric in size, necessitating the use of *4D synchrotron X-ray nanoimaging*. Consequently, various synchrotron X-ray imaging techniques are presented, with a particular emphasis on those leveraging the coherent properties of synchrotron radiation, which are better suited for 4D nanoimaging. The five stringent requirements necessary for obtaining relevant results to investigate early age cement hydration are thoroughly discussed. Following this, examples of such studies are presented, highlighting the key data that can be obtained. Both the advantages and current limitations of these techniques are addressed. Particular emphasis is placed on the spatial dissolution rates of alite, which seem to be strongly dependent on the initial particle sizes. Additionally, descriptors related to the C−S−H gel shells, such as growth rate and densification over time, are provided. Unfortunately, to date, 4D nanoimaging lacks the temporal and spatial resolution required to measure the growth rates of C−S−H gel needles. However, optimized beamlines at fourth-generation synchrotron sources are expected to enable these types of studies in the near future.

In the final section, future perspectives are presented. Initially, the technical specifications necessary to investigate the transition from the accelerated to decelerated cement hydration stages are discussed. The key requirements are a temporal resolution better than 100 min concurrent with a spatial resolution of 100 nm. Upon meeting these technical objectives, the mechanistic role of admixtures in accelerating low-carbon cement hydration could be elucidated, and the mechanical strengths at early ages are expected to be further enhanced.

The accompanying image is an artistic view and it is explicitly stated that 4D nanotomography is performed on capillaries filled of commercial cement pastes and not on concrete samples.

1. BRIEF INTRODUCTION TO CEMENT AND CEMENT HYDRATION COMPLEXITY

Concrete is the largest manufactured product and ranks as the second most utilized commodity, following freshwater. Portland cement (PC),[1] which is mainly based on Portland clinker, is the primary component of concretes, with global production reaching 4.2 gigatones (Gt) in 2022.[2] On average, the

Received: January 20, 2025
Revised: April 24, 2025
Accepted: May 7, 2025
Published: May 29, 2025

https://doi.org/10.1021/accountsmr.5c00018
Acc. Mater. Res. 2025, 6, 814−827

production of one ton of clinker results in the emission of ≈850 kg of CO_2 into our atmosphere,[3] due to limestone decomposition and fuel combustion. This corresponds to ≈8% of the total anthropogenic CO_2 emissions.[4] If cement production were considered a country, it would rank as the third largest emitter, following China and the USA. Consequently, reducing the CO_2 footprint of cements has been identified as a critical societal need,[5,6] leading to numerous proposals for low-carbon cements. Here, I focus on the most significant category: binders with a reduced Portland clinker factor achieved by partially replacing fast-reacting PC with comparatively slower-reacting supplementary cementitious materials (SCMs).[7] In order to have the CO_2-footprints as low as possible, new types of cements are being allowed in the standards, such as CEM II/C-M authorized in the European Union in 2021, which permits up to 50% of Portland clinker to be replaced. However, these low-carbon cements exhibit lower mechanical strengths at 1 day compared to the PCs currently in use. Understanding early age cement hydration is crucial for mechanistically enhancing and accelerating cement hydration, with the ultimate goal of increasing the one-day mechanical strengths. It should be noted that concrete in real-world applications requires several days of curing before the formworks can be removed. The specific times depend on the type of concrete and the intended use. One-day strength is the most common proxy to ensuring the target mechanical strengths at the required (early) age.

Gray Portland clinker is fabricated at ≈1450 °C and it contains two calcium silicate solid solutions − impure alite as it typically contains MgO, Na_2O and Al_2O_3 (simplified Ca_3SiO_5 or C_3S), and impure belite (simplified Ca_2SiO_4 or C_2S) − as well as two calcium aluminate solid solutions − tricalcium aluminate (simplified $Ca_3Al_2O_6$ or C_3A) and ferrite (simplified $Ca_4Al_2Fe_2O_{10}$ or C_4AF). PCs are produced by milling the clinker with the setting regulator − calcium sulfate(s) − and limestone (simplified as $CaCO_3$). Hence, cements are multi-mineral materials, each phase with variable chemical composition, due to elemental impurities, and a broad range of particle sizes. Furthermore, there is a growing trend of using (i) inorganic additions (i.e., SCMs) with diverse mineral contents and textural characteristics, and (ii) chemical, mainly organic, admixtures to tailor engineering properties. Low-carbon cements are highly complex, typically containing seven crystalline phases − C_3S, C_2S, C_3A, C_4AF, CaO, $CaSO_4 \cdot 2H_2O$, $CaCO_3$ − from the PC, along with several crystalline phases and at least one amorphous phase from the SCM addition.

After cement is mixed with water, setting and hardening processes occur. This stunning transformation−from a liquid that can be shaped by formwork to a solid load-bearing material−enables to build structures that contribute to healthier, safer and more comfortable and secure environments. The cement hydration reactions are very complex. Following partial dissolution, mass transport and supersaturation, interconnected processes of dissolution, crystallization and precipitation occur. The nucleation and growth of hydrated phases can occur through heterogeneous (on surfaces) or homogeneous (within the pore solution) pathways, and these processes may follow either classical or nonclassical crystallization mechanisms.[8] In low-carbon cements, more than three hydrated crystalline phases − ettringite, AFt or $Ca_6Al_2(SO_4)_3(OH)_{12} \cdot 26H_2O$; portlandite, CH or $Ca(OH)_2$; and hemicarboaluminate, Hc or $Ca_4Al_2(OH)_{13}(CO_3)_{0.5}(H_2O)_{5.5}$)− and usually three disordered phases − C−S−H gel or $\approx (CaO)_{1.8}SiO_2(H_2O)_{4.0}$; C−(A)−S−H gel or $\approx Ca_{1.5}Al_{0.2}SiO_{3.8}(H_2O)_{4.0}$; and iron-siliceous hydrogarnet, Fe−Si−hg or $\approx Ca_3Fe_2(SiO_4)_{0.84}(OH)_{8.64}$) − are formed. The stoichiometries given here for C−S−H and C−(A)−S−H are very simplified, as they largely vary depending upon cement initial composition and the hydration experimental conditions. For an in-depth understanding of the hydration processes in cements, comprehensive resources are available, including books[1,9] on cement chemistry and specialized texts on characterization techniques.[10−12]

Next, the chemical and compositional complexity of building materials should be briefly mentioned as it is the key reason to use the X-ray imaging techniques. (1) Portland clinker, coming out of every kiln, is at the heart of low-carbon cement fabrication because it ensures homogeneous performances and fast hydration. (2) Type I Portland cement is fabricated by adding the setting regulator (calcium sulfates) and milling to an ever-increasing finesse. (3) Low-carbon cements are fabricated by partial replacement of PC (in Europe), or addition to the ready-mix (in USA), by limestone filler and SCMs (i.e., blast furnace slags, fly ashes, natural pozzolans, calcined clays, vegetable ashes, etc.). (4) Several chemical admixtures (mainly organic) are added to modify properties like the rheology at very early ages and to tailor reaction some hydration rates (these chemicals belong to the following nonexhaustive list of families: super-plasticizers, accelerators, retarders, defoaming, air-entraining agents, self-healing polymers, corrosion inhibitors, waterproofing membranes and fibers). (5) The setting and hardening of hydrating cement pastes can be carried out under a number of variables that modify the final performances like water-to binder mass ratio (w/b), temperature, pressure, etc. Here it should be mention than additional CO_2 curing for a short period of time could yield lower carbon footprint(s) of the resulting building materials. (6) So far, the mixes refer to pastes. Mortars are fabricated when sand is added to the hydrating mixtures. The sand can be natural, or arising from recycled materials, or even carbonated recycled materials. (7) Finally, concretes are prepared by adding gravel of different sizes that again can be natural or arising from (carbonated) recycled materials. X-ray CT, to be detailed in section 3, is very well suited to nondestructively study processes taking place in these very heterogeneous materials. This is the core of 4D (3D + time) X-ray imaging: to quantitatively measure microstructural changes with time. The main processes that are being investigated are hydration, shrinkage, carbonation, cracking under mechanical loads and deterioration because the exposure to harmful species such as Cl^-, SO_4^{2-} and CO_2, or to other conditions like high temperatures or alkali-silica reactions. Selected key features that are being mapped out by μCT during these processes are (i) porosity evolution and clinker particle dissolution rates during hydration; (ii) micro- and mini-cracks development under mechanical loads; (iii) carbonation cracking during CO_2-curing; and (iv) porosity evolution during durability studies, just to mention a few.

Furthermore, the applications of cements are primarily in concretes and mortars. Here, the discussion is limited to cement pastes, while acknowledging the challenges involved in translating knowledge from pastes to mortars and concretes. Moving forward from 4D microimaging to 4D nanoimaging, it is important to discuss how the study cement pastes with the highest possible spatial resolution could affect/improve the concrete performances. This is work in progress. I anticipate that the following descriptors, studied as a function of cement finesse and organic admixture addition, could be very important to

https://doi.org/10.1021/accountsmr.5c00018
Acc. Mater. Res. 2025, 6, 814−827

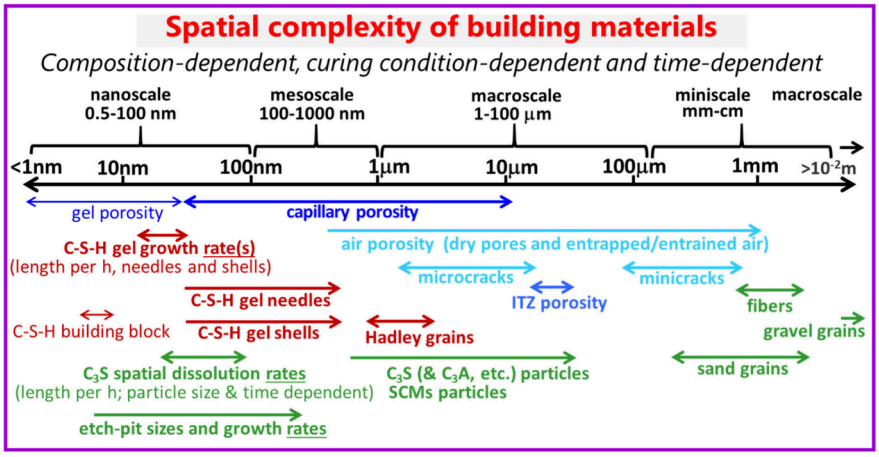

Figure 1. Scheme illustrating the spatial heterogeneity and complexity of building materials. A nonexhaustive set of features is highlighted including their relevant length scales. Porosity (blue and pale blue): water-gel, pore solution porosity, dry pores, entrapped air, entrained air and ITZ additional porosity. Anhydrous particle size (green): C_3S (and other clinker components), SCMs, sand and gravel. Hydrates (mainly but not only C−S−H gel) are plenty of features at different scales (brown): basic building blocks, shells, needles and Hadley grains for C−S−H gel. The size of other hydrates such as portlandite and ettringite are not given for the sake of simplicity. Moreover, X-ray nanoimaging data allows to measure spatial dissolution rate(s) of (dissolving) anhydrous components [such as C_3S, C_3A or metakaolin] and spatial growth rate(s) of (precipitating) hydrated components [such as C−S−H gel or ettringite] from time-lapse data.

understand and predict the hydration rates. (i) C_3S spatial dissolution rate as a function of the initial particle size; (ii) alite etch-pit growth rate; (iii) C−S−H gel shells around alite particles as thin and porous as possible; (iv) to maximize the ratio outer product versus inner product C−S−H gel. In turn, if we accelerate the early age hydration rates, we could decrease the clinker factor (increase the SCMs amount per cubic meter of concrete) as one of the main limiting factors nowadays of the low-carbon cements is their low mechanical strengths at 1−3 days of hydration.

In addition to their chemical and compositional complexity, building materials are extremely heterogeneous, see Figure 1. In mortars and concretes, additional heterogeneity arises from the sand and the gravel. Here, special attention should be given to the interfacial transition zone (ITZ), the region of cement paste surrounding the aggregate particles, which has locally increased porosity due to packing effects.[13] Restricted to cement pastes, porosities span 6 orders of magnitude, ranging from water gel pores with a minimum size of ≈1 nm to entrapped air with a maximum size of ≈1 mm. After mixing with water, capillary pores exhibit sizes of the order of several microns, enclosing the cement particles. As hydration progresses, these pores become partially filled with hydration products and gradually evolve to smaller sizes filled with water-vapor, i.e. pore-drying.[14] Regarding the anhydrous particles from PCs and SCMs, they exhibit varying size distributions and dissolve at significantly different spatial rates, see Figure 1. In geochemistry, it is well established that, for a given crystalline phase, the dissolution rates are strongly influenced by the particle size.[15] C−S−H gel from PC hydration and C−(A)−S−H gel from the pozzolanic reaction are intrinsically heterogeneous. C−S−H gel exhibits features spanning 3 orders of magnitude, from the smallest building blocks of approximately 5 nm to Hadley grains of around 3 μm − hollow-shell structures formed in the spaces originally occupied by small alite particles. Key characteristics include C−S−H gel shells/rims, which are layers that precipitate and thicken over alite surfaces, and C−S−H gel needles. Moreover, inner product (the C−S−H gel that is formed within the boundary region of the anhydrous cement grain) and outer product (the C−S−H gel that is formed in the originally pore solution-filled volumes) have slightly different chemical compositions, densities and binding performances.[16] Inner product C−S−H gel is generally related to the shells/rims and outer product C−S−H to the needles. However, it is noted that the morphology of C−S−H may depend on the technique used for its characterization and it usually presents fibrillar morphology when observed by TEM.

2. EARLY-AGE CEMENT HYDRATION

The hydration of PC can be studied by analyzing the heat released by the chemical reactions. Calorimetry, while representing a composite signal of all these processes (dissolution and precipitation), is highly illustrative and experimentally robust. Its widespread use further enables reliable comparisons. Figure 2 shows the typical isothermal heat flow trace of a hydrating cement at early ages and it can be considered that cement hydration takes place in five stages.[17] The initial fast dissolution (a few minutes, ①) stage, i.e. wetting, is followed by an induction period (≈2 h, ②) that can be strongly

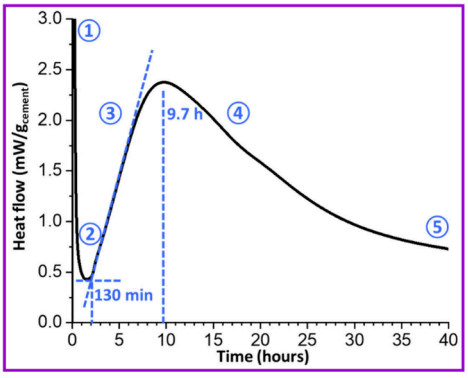

Figure 2. Typical heat flow trace for a PC 42.5N paste (water to cement mass ratio (w/c) of 0.50 at 20 °C) during the first 2 days. The end of the induction period, ≈130 min, and the maximum of the heat flow curve, ≈10 h, are highlighted. For the meaning of the numbers, see the text.

https://doi.org/10.1021/accountsmr.5c00018
Acc. Mater. Res. 2025, 6, 814−827

modified by the additions and the admixtures. During this time, hydration reactions are occurring but with very slow rates. Then, the acceleration period develops (several hours until the maximum in the heat flow trace, ③), which is followed by the deceleration period (tens of hours, ④). Finally, cement hydration enters in a diffusion-controlled stage (weeks-months to years, ⑤) because the lack of liquid pore solution close to partly reacted particles. It is now agreed that dissolution controlled by undersaturation is the mechanism responsible of the induction period, ②,[18] and not the protective membrane theory. Conversely, there is still no agreement in the mechanism to explain the transition from acceleration to deceleration, i.e. ③→④, when there is (i) a degree of hydration of just 10−20% of the PC (≈20−25% of C_3S depending upon the finesse of the PC), (ii) a lot of pore solution available, and (iii) plenty of space for the hydrates to grow.

The most advanced theories[19] are based on heterogeneous nucleation and growth within confined regions taking into account the initial particle size distributions,[20] for instance, the reaction zone.[21,22] There are alternatives[23] such as the needle model[19] where C_3S hydrates[24] to yield C−S−H gel.[25] Neither the dissolution of small grains, nor etch-pits coalescence, nor C−S−H gel growth rate slowdown by impingement, nor water diffusion − alone− can currently explain the transition from the acceleration to the deceleration periods,[17] see Figure 2. The following factors may play a significant role in explaining the ③ → ④ $_{\text{transition:}}$ (i) C_3S spatial dissolution rate that seems to be particle size dependent; (ii) etch-pits[26] growth and coalescence; (iii) the consequences of the pore solution-filled gap which opens between the dissolving (inward) C_3S grains and the growing (outward) C−S−H gel shell;[27] (iv) overall fraction of the total alite surface covered by C−S−H gel shell; (v) C−S−H gel shell spatial growth rate; (vi) C−S−H gel shell mass density evolution with time; and (vii) C−S−H gel needle spatial growth rate.

During cement curing, the microstructures evolve alongside changes in both crystalline and amorphous phases. Crucially, the evolution of the microstructures during hydration modifies the diffusion of species such as Ca^{2+}, OH^- and $H_2SiO_4^{2-}$. Therefore, phase assemblages (type and reaction products forming) and microstructure development are intimately connected. This interplay partly explains the complexity of the curing behavior in cementitious materials. Thus, measuring the evolution of phase assemblage by *in situ* laboratory[28] and synchrotron[11] powder diffraction is very important. However, these techniques produce volume-averaged results that overlook spatial characteristics, such as particle size dependence, diffusion barrier appearance, or C−S−H gel needle impingement. On the other hand, there are several electron microscopy modalities and SEM and TEM are the most widely used in the characterization of cement hydration. In particular, TEM and some of its variants (such us FIB-TEM, STEM, etc.) provide data with very high spatial resolution. However, they cannot analyze relatively thick samples and cannot follow changes with hydration time under relevant conditions. For instance, *in situ* liquid cell TEM was used to study PC hydration but the paste was confined between two silicon nitride membranes with a distance of 250 nm.[29] The PC was extensively milled to have extremally small particles fitting within the cell and the w/c ratio used was as high as 15. These are not relevant conditions. In addition, water-rich samples subjected to the electron beam suffer from damage such as water loss and alterations of the microstructures. This makes TEM unsuitable for the time-lapse microstructural characterization of hydrating cements. Therefore, the visualization of the evolving cement hydrating microstructures by 3D X-ray imaging (computed tomography, CT)[30] is becoming vital for understanding the hydration mechanisms. The key advantages of μCT and nCT are the absence of sample conditioning (that can alter the specimens during the preparations) and its nondestructive nature during measurements (although possible radiation damage should be checked for synchrotron experiments).

3. X-RAY NANOIMAGING OF CEMENTS

The spatially resolved characterization of hydrating and hydrated cements is increasingly recognized as essential.[12,31,32] Within this field, X-ray microcomputed tomography (μCT, in their different modalities such as absorption-contrast, phase-contrast and diffraction tomography, among others) of cementitious materials is gaining traction as evidenced by the reviews published in the last five years.[33−37] Many features can be followed, but here, I fully focus on the analysis of hydrating cement pastes by hard X-rays.

There are many techniques that permit the extraction of 3D information by a tomographic approach, where a virtual volume is reconstructed from hundreds (or thousands) of angular projections (i.e., 2D detector images acquired at each tomographic angle). In turn, 3D imaging techniques can be classified in full-field microscopies, where an angular projection is taken at once, and scanning microscopies, where an angular projection is recorded from the combination of many measurements by raster scanning the sample with a tiny beam. The interested reader is addressed to the imaging chapter of a standard synchrotron book.[38] For phase-contrast imaging, there are six experimental approaches for attaining the required information: (1) Propagation-based imaging; (2) Modulation-based (also known as speckle-based); (3) Grating interferometry; (4) Analyzer-based; (5) Edge illumination; and (6) Mesh-based. These techniques have different experimental set-ups, and importantly, also different data processing approaches.[39] Propagation-based tomography is undoubtedly the most used experimental setup. Moreover, to increase the spatial and contrast resolution, holographic X-ray computed tomography (HXCT) can be used. In this approach, a (partly) coherent beam passes through the sample and propagates a given distance before being measured at the detector position. Several detector images, taken with various distances of propagation, allow an accurate reconstruction of the interior of the sample.

Additionally, there is a set of lensless imaging techniques where ptychographic X-ray computed tomography (PXCT)[40] is framed. These techniques[41] merge scanning X-ray microscopy and coherent diffraction imaging to yield imaging data of unprecedented spatial and contrast resolution by also reconstructing the X-ray probe. Being a scanning technique, the time resolution is not fast.

Because the heterogeneity of hydrating cements is so pronounced, see Figure 1; the best possible spatial resolution is required, i.e. X-ray nanoimaging. Here, a word of caution is needed concerning spatial resolution and voxel size. For attenuation-based, or propagation-based phase-contrast, synchrotron μCT, working with parallel X-rays, the voxel size depends upon the 2D detector physical pixel size and the magnification system used. For other modalities such as those employing divergent X-rays, the voxel size also depends upon the optics configuration. However, due to radiation damage, mechanical instabilities (sample and/or optics), poor signal-to-noise ratio (SNR), and other error sources, the spatial resolution

https://doi.org/10.1021/accountsmr.5c00018
Acc. Mater. Res. 2025, 6, 814−827

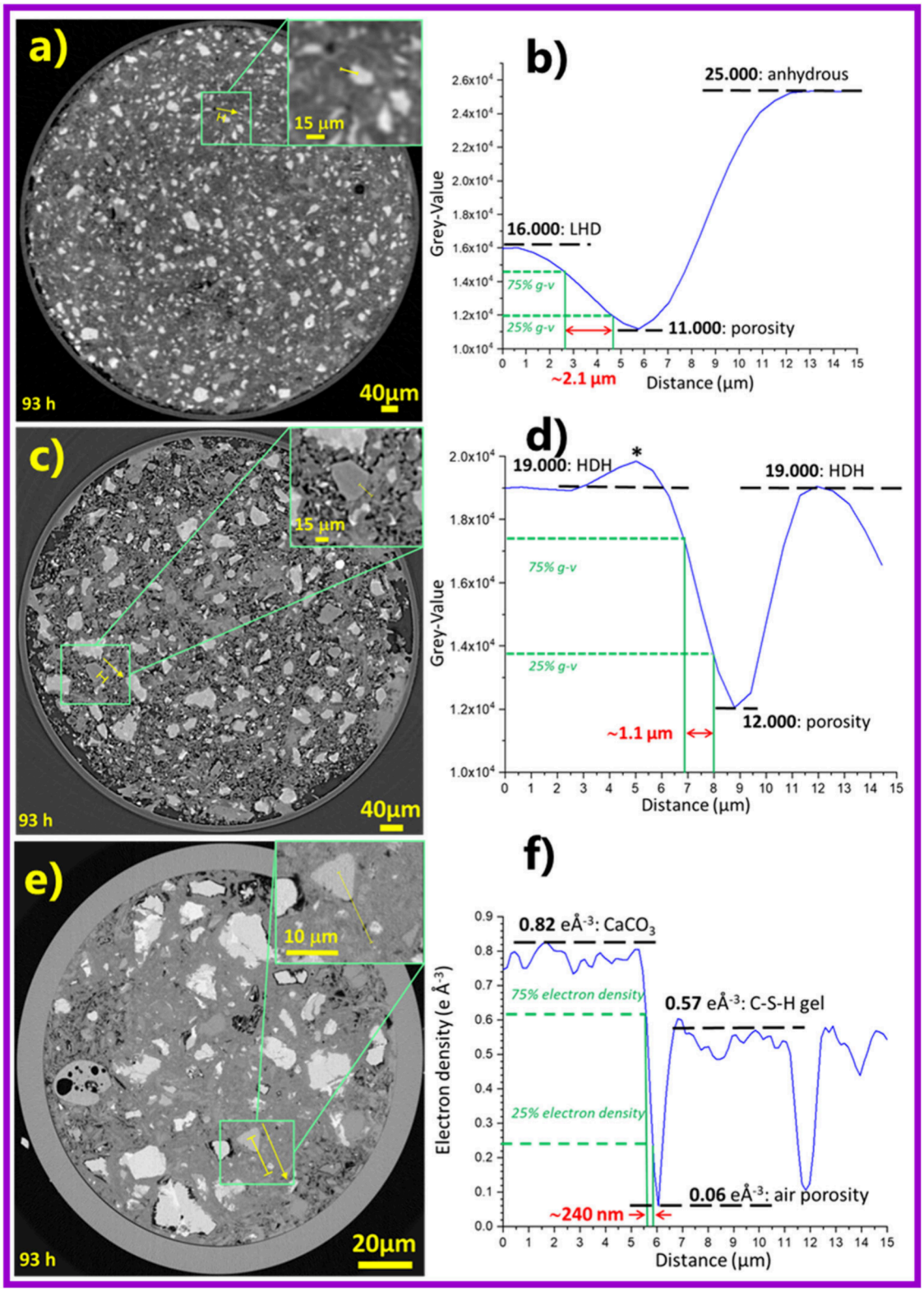

Figure 3. Selected views of three X-ray imaging studies for PC pastes. (a) Selected orthoslice and (b) gray-value profile of the yellow line (shown in the left panel) including a sharp interface for the laboratory μCT study (PC-52.5 paste with w/c = 0.40). FoV = 1200 × 940 μm (H × V), number of projections = 1637, voxel size = 1.0 μm, total time = 3.5 h. (c) Selected orthoslice and (d) gray-value profile of a sharp interface, as previously described, for propagation-based phase-contrast, synchrotron μCT study (PC-52.5 paste with w/c = 0.50). FoV = 800 × 1190 μm (H × V), number of projections = 6000, voxel size = 0.65 μm, total time = 5 min. (e) Selected orthoslice and (f) electron density profile of a sharp interface for nf-PXnCT study (PC-52.5 paste with w/c = 0.50, data set at 4 days of hydration). FoV = 186 × 30 μm (H × V), number of projections = 420, voxel size = 186.6 nm, total time = 3 h. Adapted with permission from reference 46. Copyright 2023 The Authors.

https://doi.org/10.1021/accountsmr.5c00018
Acc. Mater. Res. 2025, 6, 814−827

can be worse, about 2 to 10 times poorer than the voxel size.[30] There is no universally adopted figure of merit for estimating the spatial resolution in 3D, but two approaches are becoming increasingly used:[42] (i) Fourier-Shell-Correlation,[43] and (ii) edge sharpness across selected interfaces. This second approach is based on ISO/TS 24597 "Microbeam analysis - Scanning electron microscopy - Methods of evaluating image sharpness"[44] which estimates spatial resolution as the change between 25%−75% gray value along the studied interface(s).[45]

I define X-ray nanoimaging, for the purpose of this discussion, as studies reporting data with a spatial resolution better than 0.5 μm (500 nm). The spatial resolution is related, but not directly proportional, to the voxel size. Hereafter, μCT refers to synchrotron phase-contrast microcomputed tomography or just microtomography. nCT refers to nanocomputed tomography or just nanotomography. Figure 3 displays three X-ray imaging works where the spatial resolution is estimated by the edge sharpness approach. Figure 3a displays a typical laboratory attenuation-based μCT with a voxel size of 1.0 μm and a spatial resolution of ≈2.1 μm. Figure 3c shows a synchrotron phase-contrast μCT with a voxel size of 0.65 μm but a spatial resolution of ≈1.0 μm. Although the voxel size is submicrometric, this is not a nanoimaging investigation. Conversely, Figure 3e shows a synchrotron nf-PXnCT with a voxel size of 186.6 nm and a spatial resolution of ≈250 nm. This is considered here a nanoimaging study.

The next section moves to 4D nanoimaging which can help to better understand the cement hydration processes taken place at early ages, see Figure 2. In these 4D studies (time-lapse), the trade-offs when selecting the experimental details are more severe because both time resolution and space resolution are critical, see Figure 4. For the target time resolution, and in addition to the best possible compatible spatial resolution, other features must be considered. Because of the experimental configuration and the current detector features, the Field of View (FoV) of a single measurement is typically ≈2000 times larger than the size of the reconstructed voxel, as the most commonly used advanced detectors currently have 2048 × 2048 pixels. Scanning techniques could allow larger regions to be studied, but the total data acquisition is long. This may have consequences for the extraction of the desired information, such as the hydration behavior of different particle sizes of different components, since the (nano)imaged volume may not be large enough for that particular feature. For samples larger than the FoV, stitching (a method that combines two or more data sets into a unified one) can be used, but the overall acquisition time increases, which may not be suitable for time-lapse experiments. A second possibility is to use the half acquisition mode, where the center of rotation is shifted close of the edge of the detector. This approach combines the projections taken from 0 to 180 deg with the other half captured from 180 to 360 deg, ultimately forming a virtual volume with twice the FoV allowed by the detector used. To the best of my knowledge, this method has not been applied in studies of cement hydration imaging. Moreover, and for a given time and spatial resolution the image quality of the reconstructed virtual volumes can be evaluated by determining the SNR and the contrast to noise ratio (CNR). The higher the SNR and the CNR, the better image quality in the virtual volumes. The SNR can be estimated by the ratio of the mean gray level value (or the mean electron density) of the voxels studied to the standard deviation of the gray level value of the voxels in the background.[47] Similarly, the CNR can be estimated by the difference of the mean gray value of the voxels of the studied component and the background (i.e., air) voxels over the standard deviation of the gray level value of the voxel of the studied component.[47] SNR and CNR are key parameters that may allow distinguishing between relatively similar components, or not. It is noted that different nCT techniques have different intrinsic CNR and acquisition times. For instance, 3D scanning microscopies require much longer experiments but usually offer better contrast between the different components (i.e., contrast resolution). Finally, the X-ray nanoimaging experiment should allow relevant conditions to be investigated like water-to-binder ratios close to 0.4−0.5 or the addition of chemical admixtures.

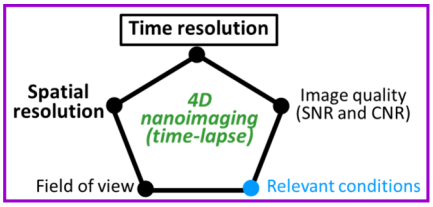

Figure 4. Main elements for planning synchrotron 4D X-ray nanoimaging experiments of cement hydration. The chief feature is the time resolution that may impose constraint(s) to the second most important aspect, the spatial resolution. Other characteristics also play important roles and they must be carefully selected, such as to ensure enough contrast between different components to distinguish the growing hydrates and large enough field of view to prepare relevant samples.

4. 4D X-RAY NANOIMAGING OF EARLY-AGE CEMENT HYDRATION

To gain a deeper understanding of the requirements for time resolution in 4D nanoimaging studies, Figure 5 displays the isothermal calorimetry traces of two PC pastes and two low-carbon cement pastes. Comparison of PC and low-carbon cement traces reveals that hydration kinetics are accelerated due to the filler effect,[48,49] resulting from the additional surfaces introduced by the incorporation of the SCM. Additionally, the use of a C−S−H nucleation seeding admixture further accelerates these processes,[50−52] which is crucial for achieving adequate mechanical strength at 1 day of hydration. The alite peak maxima can occur as early as 5 h, highlighting the need for a time resolution of 100 min or better.

It is acknowledged that there are many works in 4D microimaging of cement hydration.[11,34] and that there have been recent developments such as (i) the automated correction for the displacement of suspended microparticles at very early ages;[53] (ii) quantitative measurements of the fast dissolution of plaster and the gypsum precipitation;[54] and (iii) the alite particle dissolution measurements by fast synchrotron phase-contrast nCT.[45] However, none of these 4D imaging works combine simultaneously the five stringent requirements needed for the mechanistic understanding of cement hydration at early ages, which are given in Box 1.

In particular, synchrotron phase-contrast μCT lacks both the required spatial resolution and sufficient component contrast, failing to meet criteria (3) and (5). While, attenuation-contrast and phase-contrast synchrotron nCT, within a multiscale approach, can satisfy criterion (5), it does not comply with criterion (3). (3) is essential for classifying hydrates and tracking the time-evolution of C−S−H gel. For instance, this is the case of 4D nanotomographic studies on the sintering of metals and

https://doi.org/10.1021/accountsmr.5c00018
Acc. Mater. Res. 2025, 6, 814−827

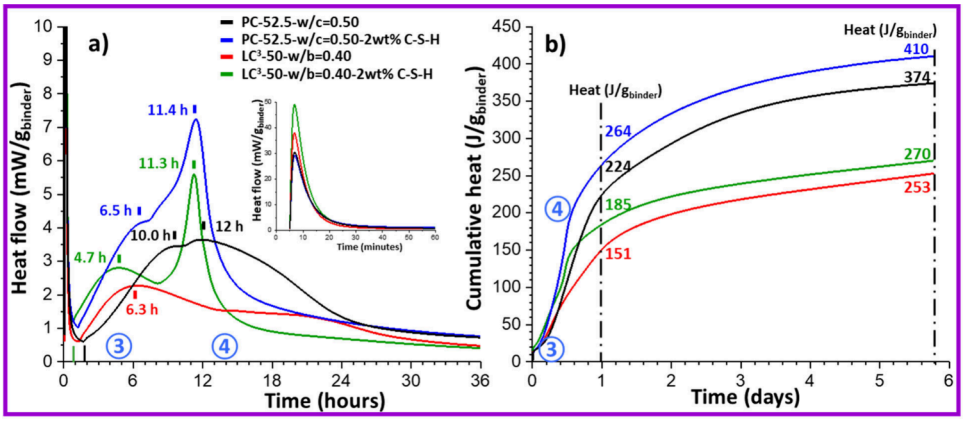

Figure 5. Isothermal calorimetries (T = 20 °C) for four typical cement pastes without superplasticizers, with values referenced to the mass of dry binder, showing the effects of a strength-enhancing admixture (in this case based on C−S−H nucleation seeding). Samples: PC 52.5R, $D_{v,50}$ = 10.3 μm, Blaine = 466 m^2kg^{-1}, SO_3 = 3.3 wt % [black traces]; the previous PC with 2 wt % of Master X-Seed STE53 [blue traces]; Limestone Calcined Clay Cement (LC^3): 53 wt % of this PC, 30 wt % of a kaolinitic calcined clay ($D_{v,50}$ = 12 μm, specific surface area: 4.0 m^2g^{-1}, ≈40 wt % of metakaolin), 15 wt % of limestone ($D_{v,50}$ = 5.0 μm) and 2 wt % of gypsum ($D_{v,50}$ = 13.0 μm) [red traces]; the previous LC^3 with 2 wt % of Master X-Seed STE53 [green traces]. (a) Heat flow curves up to 36 h for better visualization. The times for the maxima of the alite and aluminate peaks are given. The end of the induction period ranges 50 to 110 min. The inset shows the heat flows during the first hour, stage ① in Figure 2. (b) Cumulative heats developed during the first 6 days of hydration. The total heats (J/g) at 1d and 6 d of hydration are explicitly given.

Box 1. Five stringent requirements are needed for relevant 4D X-ray nanoimaging of cementitious materials at early hydration ages, i.e., first two days of hydration.

(1) To be able to investigate pastes with w/c≈0.30-0.60 (i.e. relevant conditions #1). The mechanisms of nucleation and growth, as well as the morphologies of some products, are different for higher w/c ratios. The growth of the hydrates must occur in confined space(s).

(2) To be able to probe sufficiently large volumes, i.e. a minimum of 150 µm, to allow cement hydration with the particle sizes of commercial materials (i.e. relevant conditions #2). From a scientific point of view, further milling of commercial cements to fit within very small capillaries for *in situ* hydration using nanoimaging works well. However, it provides very misleading information for engineering implications by overestimating hydration rates. Additional grinding of commercial samples should be avoided.

(3) Good contrast resolution to be able to identify the different evolving components (f.i. C-S-H gel from other hydrates) and to measure the C-S-H gel densification with time.

(4) Fast time resolution, about 100 min or faster, to be able to study the acceleration period, see process ③ in Figures 2 and 5.

(5) Best possible spatial resolution, ideally better than 100 nm.

alloys where a time resolution better than 45 min is already attained. Synchrotron soft X-ray nCT[55] meets (3) and (5), but it requires very large w/c ratios and very small FoV which prevent hydrates to growth in conditions relevant to practical applications − failing to meet criteria (1) and (2). It is noted that studies on the minimum representative volume element (RVE) for nanotomography of cements have not yet been performed. The sample size of 150−200 μm is the compromise between the narrowest capillaries that yield reproducible paste preparations and the maximum size for current algorithms to robustly retrieve the phases. In addition, RVE will be different for different extracted features. It could be lower than 150 μm to determine the average thickness of C−S−H shell gel, but it is likely higher than 300 μm to obtain quantitative segmentation results for the different components.

To date, only near-field ptychographic nanocomputed tomography (nf-PXnCT) fulfills all five requirements.[46] However, the best reported time resolution was 3 h, which allowed the study of the deceleration stage but not the acceleration stage. Additionally, the best spatial resolution achieved was 250 nm, which should be further improved.

The first 4D nanoimaging study of a cementitious sample was reported in 2017.[56] In this work, a model paste composed of ye'elimite ($Ca_4Al_6O_{12}SO_4$) and gypsum ($CaSO_4{\cdot}2H_2O$) was imaged by ff-PXnCT, see Figure 6. The experiment configuration at that time, far-field, only allowed imaging of a limited FoV in the horizontal direction (≈70 μm), which did not fully meet the requirement (2) above. Moreover, the time resolution was 5 h per tomogram. There were two key outputs. First, the ye'elimite spatial dissolution rate in the deceleration period, between 48 and 63 h, was estimated as ≈120 nm/h, see Figure 6. Second, the ettringite spatial growth rate during the same period, was ≈60 nm/h.

The breakthrough in 4D nanoimaging of cement hydration came with the tailoring of nf-PXnCT to cements, which allowed us to measure larger samples in a time-effective manner.[46] The

https://doi.org/10.1021/accountsmr.5c00018
Acc. Mater. Res. 2025, 6, 814−827

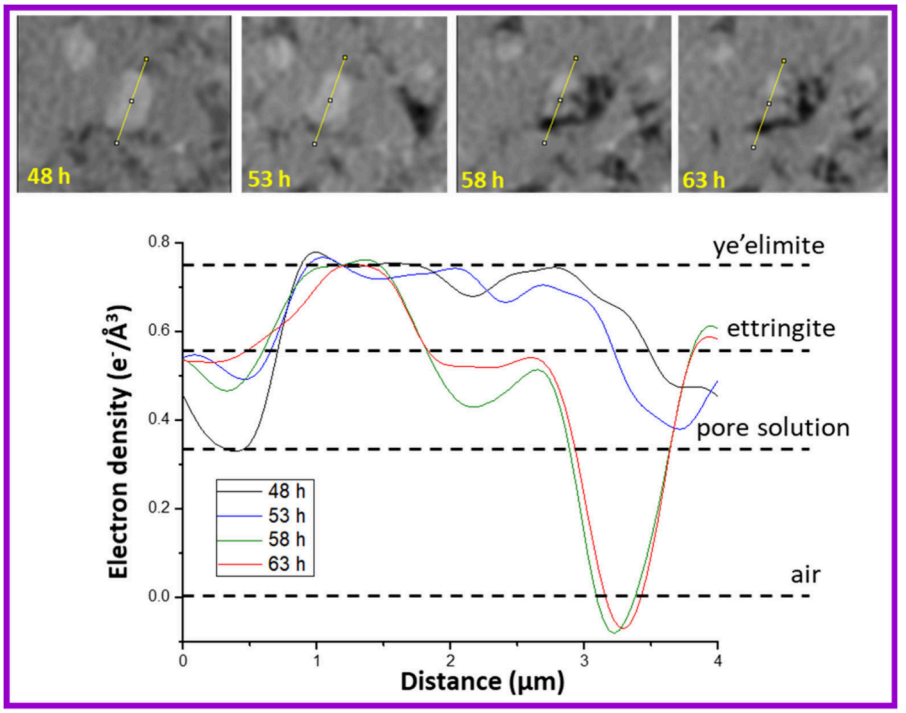

Figure 6. (Top row) 4D ff-PXnCT nanoimaging study of a paste composed of ye'elimite and gypsum pure-phases at the indicated hydration times, cSAXS BL at PSI, E = 6.2 keV, FoV = 72 × 45 μm, number of projections = 600, voxel size = 40.8 nm, total time per nCT = 5 h. (Bottom panel) Electron density profiles along the yellow lines to show the dissolution of a ye'elimite particle and the development of air-filled porosity. Adapted with permission from reference 56. Copyright 2017 The Authors.

spatial resolution was a bit poorer than in far-field configuration but relevant conditions could be met. The horizontal sample size can be now 200 μm which ensures requirements (1) and (2). The spatial resolution, for a nCT scan of 3 h, was ≈270 nm. These measurements were carried out at an PXCT optimized beamline of a third generation synchrotron source. A similar experiment at an optimized beamline in a fourth generation synchrotron source is expected to get closer to the target requirements (4) and (5). The optimized beamline should not only have much higher coherent flux at the sample position and higher optical and mechanical stability, but other features such as fast motor movements, fast detector readout, moving sample−detector distance, robust algorithms for fast phase retrieval, among others, should also be taken into account.

Here, I highlight the most important findings of our recent 4D nanoimaging study of a PC hydrating paste.[46] Figure 7 displays two selected orthoslices of the PC hydration study by 4D nf-PXnCT. At 19 h (the start of the deceleration stage because the paste had a superplasticizer), the sample contained plenty of capillary water and a C−S−H gel shell of ≈450 nm thickness and 1.51 cm^{-3} of average mass density enclosing every alite grain. The C−S−H gel shells densify with time and at 47 h its average mass density has increased to 1.71 gcm^{-3}. Moreover, Figure 7 also qualitatively shows that C_4AF regions, intergrown with C_3S particles, slowed down alite hydration as the hydration front stops as soon as the C_4AF region is reached.

The 4D nanoimaging study permitted to quantitatively study the alite spatial dissolution rates. To this end, Figure 8 shows one example of the status of the components at 19, 47, and 93 h of hydration. Electron density line profiles along selected regions permit to measure the alite dissolution and the C−S−H gel densification. At 19 h, the average spatial gap that opens between the dissolving (inward) alite grains and the growing (outward)

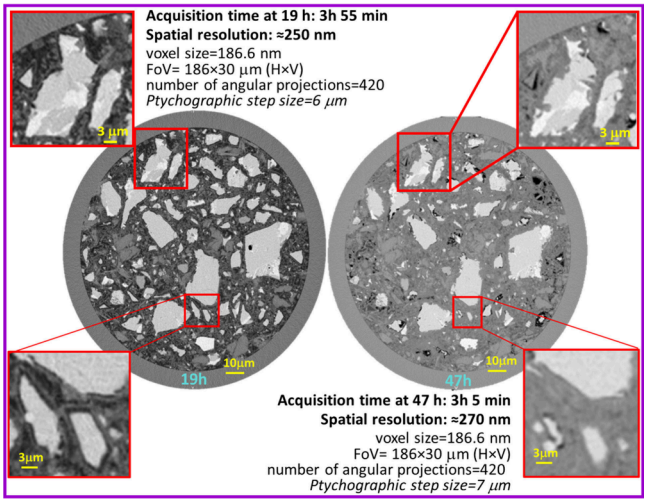

Figure 7. Selected orthoslices of the 4D nf-PXnCT nanoimaging study of a PC 52.5R paste, w/c ≈ 0.40, to qualitatively highlight the changes during hydration in the deceleration stage (i.e from 19 to 47 h). Key details of the two acquisitions are given. The enlarged views at the bottom highlight the C−S−H gel shells that surround every alite grain at 19 h and that have densified at 47 h. The enlarged views at the top are given to underline the C_4AF (i.e., ferrite) white regions which are intergrown with the alite particles. The ferrite regions are clearly identified by their electron density values, 1.06−1.10 $e^-Å^{-3}$, which are much higher than those of alite, 0.94−0.96 $e^-Å^{-3}$. The top-right panel clearly shows that hydration stops/slows down at the C_4AF interface because its much slower spatial dissolution rate. Note that the two data sets are plotted with slightly different color scales. Adapted with permission from reference 46. Copyright 2023 The Authors.

C−S−H gel shells was ≈490 nm. Other hydration features can be deduced from this 4D nanoimaging study such as the drying

https://doi.org/10.1021/accountsmr.5c00018
Acc. Mater. Res. 2025, 6, 814−827

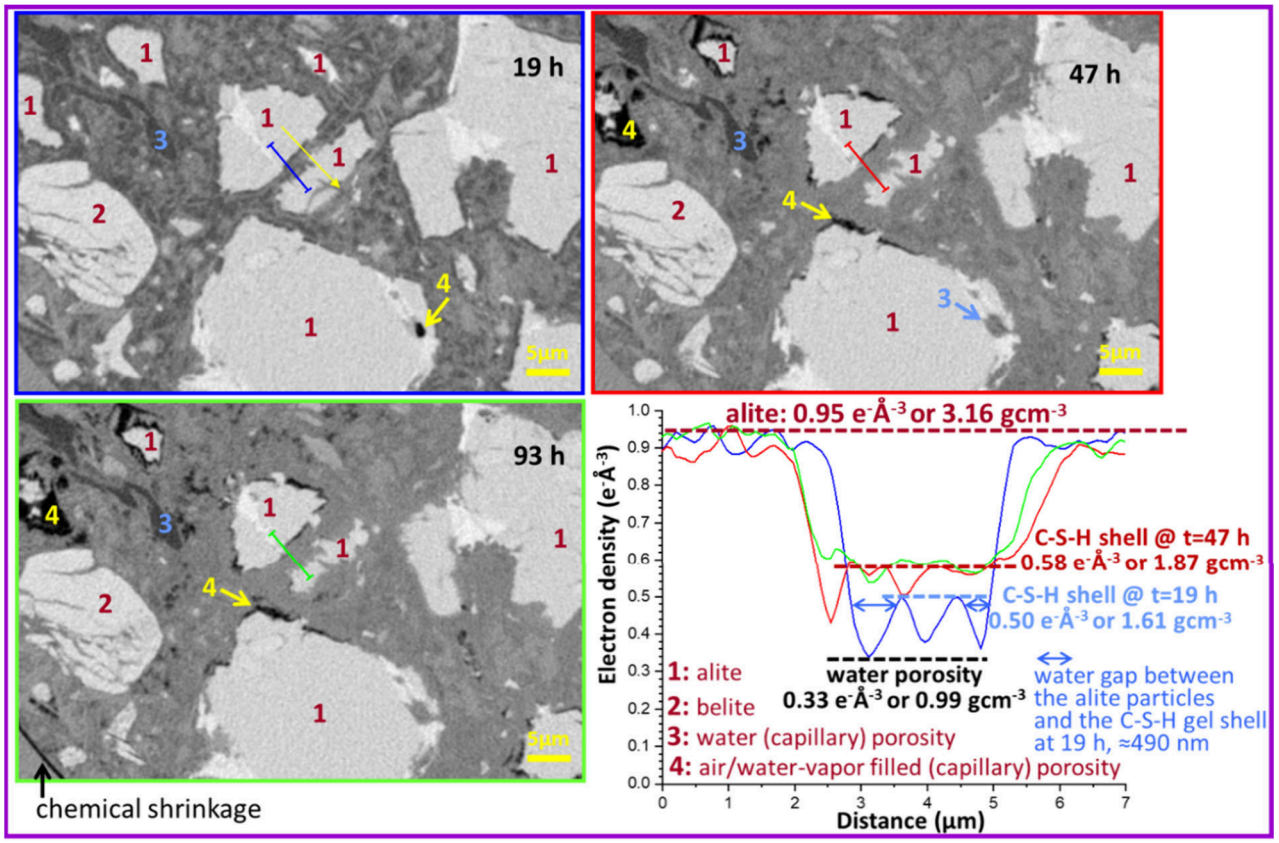

Figure 8. 4D nf-PXnCT nanoimaging study of a PC 52.5R paste, w/c ≈ 0.40, to quantitatively show the alite dissolution and C−S−H gel shell densification with time at early hydration ages. Electron density profiles are displayed in the bottom-right panel which correspond to the straight lines in the other three panels (blue at 19 h, red at 47 h and green at 93 h). The line profile at 19 h also signals the pore solution region (gap) surrounding the two chosen alite particles. The C−S−H gel shell densities are given which underlines the densification taken place between 19 and 47 h. Pore solution capillary porosity (electron density ≈ 0.33 $e^{-}Å^{-3}$) is easily distinguished from air/water-vapor filled porosity (electron density = 0 $e^{-}Å^{-3}$). Adapted with permission from reference 46. Copyright 2023 The Authors.

of the water capillary porosity (with an electron density of 0.33 $e^{-}Å^{-3}$) to become water-vapor filled with negligible electron density, see black regions in Figure 8. This identification can only be done because of the quantitativeness in electron densities of PXnCT.

Etch-pit quantification in alite is also underlined here. Etch-pit dissolution mechanism[18] is particularly relevant for conditions far from equilibrium, which is the case in cement hydration. Figure 9 shows one example where five etch-pits in an alite particle were followed.[46] In the 19 to 47 h period, the average growth rate was estimated as ≈40 nm/h. This estimation was carried out for alite particles larger than 10 μm. This rate almost doubles the alite spatial dissolution rate of flat surfaces during the same period, 25 nm/h. This emphasizes the importance and role of defects in the dissolution rates.

To end this section, Box 2 summarizes the current values of the main parameters, determined by 4D X-ray nanoimaging. They are fundamental for a better understanding cement hydration and, in particular, the transition from the acceleration to the deceleration stages.

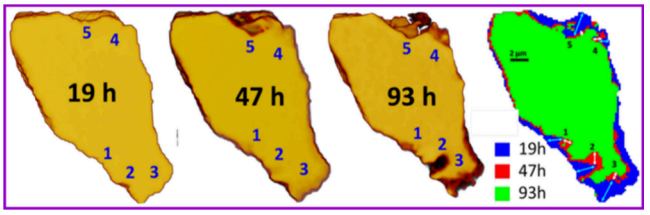

Figure 9. (Left) Hydration evolution of a ≈10 μm size segmented alite particle showing the evolution of five etch-pits at the given hydration ages from the nf-PXnCT nanoimaging study of a PC 52.5R paste, w/c ≈ 0.40. (Right) Overlay of the (2D-projected) segmented pixels to show the large variability in the growth rates of the etch-pits. Pale-blue arrows show size changes from 19 to 47 h, meanwhile white arrows display to the changes from 47 to 93 h. Adapted with permission from reference 46. Copyright 2023 The Authors.

5. PERSPECTIVE

5.1. Where We Are and Where We Should Be Going in 4D Nanoimaging of Cement Hydration

4D X-ray nanoimaging can contribute to the understanding of the cement hydration reactions/processes at early ages. However, in order to address the key transition from the acceleration to the deceleration stages, technical improvements are needed. The required advancements are depicted in Figure 10. Chiefly, the acquisition time for a full tomogram should be decreased to ≈100 min. This is dictated by the kinetics of the cement hydration as the acceleration period length ranges from 10 h to as short as 4−5 h, see Figure 5. Itself, 100 min per data set is not a big deal. However, this is a tremendous challenge when is coupled to the other key technical requirements stated in Box 1, chiefly the spatial resolution must be better than 100 nm. This

https://doi.org/10.1021/accountsmr.5c00018
Acc. Mater. Res. 2025, 6, 814−827

Box 2. Key parameters that can/could be obtained by 4D nanoimaging. The values summarized here are for the hydration of a PC 52.R paste, w/c≈0.40 and 0.43% of a polycarboxylate ether (PCE) superplasticizer, explicitly indicting the adopted assumptions, when appropriated.[46] It is noted that PCE was used to improve the paste's flowability to be able to fully fill the narrow capillaries used.

#1. Alite (C_3S) spatial dissolution rates, as a function of the initial alite particle size, in the acceleration period:

1.1. ≈100 nm/h for particles sizes smaller than 3 μm at t=0. This is an indirect measurement based on the observation of full hydration at 19 h of all alite particles with sizes smaller than 3 μm. Because the induction period ended at 4 h, due to the employed PCE, 3000 nm were dissolved in 15 h from two (opposite) dissolution fronts. This result fully agrees with previous reports.[19]

1.2. ≈33 nm/h for particles sizes larger than ≈8 μm at t=0. This is an indirect measurement based on the observation of a pore solution-filled gap of an average width of 490 nm between all particles and the C-S-H gel shells at 19 h. Under the assumption that the C-S-H gel shells only grow outwards, the dissolution rate is 490/15 or 33 nm/h. It was not possible to firmly measure if the gap width is as a function of the initial alite particle size. This information is very important for modelling.

#2. Alite spatial dissolution rate for particles larger than ≈8 μm at t=0, in the deceleration period: ≈25 nm/h. This is a direct measurement in the studied time interval 19 to 47 h. Currently, it is unknown to the author if the dissolution rate in this period is particle size dependent.

#3. Alite etch-pit growth rate(s) in the acceleration period: not measured due to insufficient time and spatial resolutions.

#4. Alite etch-pit growth rate for particles larger than ≈8 μm at t=0, in the deceleration period: ≈40 nm/h. This is a direct measurement in the studied time interval of 19 to 47 h, but is subject to a large variability. Better spatial resolution and more measurements are needed to improve the accuracy of this initial estimation.

#5. C-S-H gel shell average growth rate during the acceleration period: ≈30 nm/h. This is an indirect measurement. It is based on the average thickness of the C-S-H gel shell at 19 h, 450 nm. The underlying assumption is that the shells only grow outwards. The width of the shell is divided by the growth time, i.e. 15 h. For large alite particles, the C-S-H gel shell spatial growth rate, ≈30 nm/h, is very similar to the alite spatial dissolution rate at relatively flat surfaces, ≈33 nm/h. The C-S-H gel could be mixed with other cement reaction products. Improving the spatial resolution of 4D nanoimaging is very important to disentangle hydration products in case they are intermixed.

#6. C-S-H gel needle average anisotropic growth rate during the acceleration period: not measured due to insufficient time and spatial resolution.

#7. C-S-H gel needle average growth rate during the deceleration period: not measured due to insufficient time resolution.

#8. C-S-H gel shell/needle electron/mass density in the acceleration period: not measured due to insufficient time and spatial resolution.

#9. C-S-H gel shell electron/mass density in the deceleration period:

9.1. ≈0.47 $e^{-}Å^{-3}$ or 1.51 gcm^{-3} (average value at 19 h). Direct measurement of the electron density. Assumption of the gel stoichiometry to obtain the employed A/Z value of 1.94, which permits to convert electron densities in mass density.[57] The associated error to the conversion is quite low.

9.2. ≈0.53 $e^{-}Å^{-3}$ or 1.71 gcm^{-3} (average value at 47 h). Direct measurement of the electron density. Assumption of the gel stoichiometry but with very minor consequence in the mass density.

spatial resolution is essential to measure the C−S−H growth rates of shells and needles as well as to determine the alite (and other components) spatial dissolution rates as a function of the initial particles sizes, see Figure 10 and Box 2. It should be noted that achieving a spatial resolution better than 100 nm is nowadays common for 3D nanoimaging. In fact, we have

https://doi.org/10.1021/accountsmr.5c00018
Acc. Mater. Res. 2025, 6, 814−827

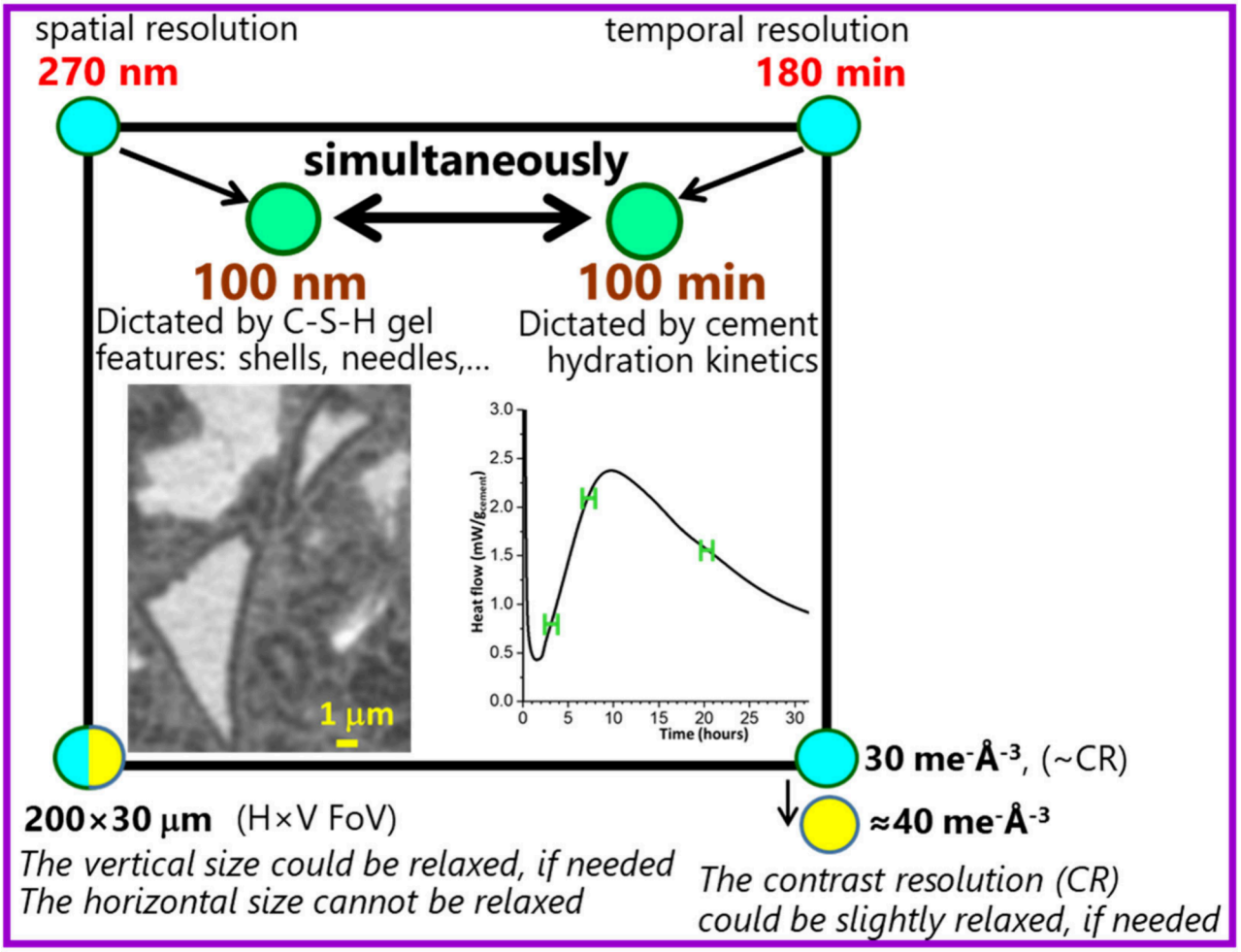

Figure 10. Schematic representation of where we are (year 2024 – features highlighted with blue circles) and where we should be going (2025–2030 – features highlighted with green circles) in 4D X-ray nanoimaging of cement hydration at early ages. The targets are (1) to decrease the time resolution to 100 min, to be able to study the key acceleration period, and *simultaneously* (2) to increase the spatial resolution to 100 nm, which is mainly imposed by the C–S–H gel characteristics to be measured: shell size and growth rate, needle size and growth rate, etc. If strictly needed, two features of the 4D nanoimaging studies could be slightly relaxed (see yellow circles). The horizontal size, ≈200 μm, cannot be narrowed as it is needed to ensure relevant sample preparation, i.e. to have an adequate distribution of all cement particles.

reported a 3D spatial resolution of 56 nm in cement pastes by far-field ptychotomography.[58] The limit of spatial resolution in 3D investigations of cement pastes is likely to be imposed by radiation damage. The challenge is to combine the best possible spatial resolution with the fastest possible measurement of large FoV images.

Attaining simultaneously: (1) 100 min of time resolution; (2) 100 nm of spatial resolution; (3) 200 μm of horizontal sample size (the largest alite grains have close to 25 μm and the volume of interest should be about 8 times the size of the largest feature); and (4) very good component contrast; is a tremendous challenge. Therefore, some sacrifices may be needed, as depicted in Figure 10. On the one hand, the vertical size of the nanoimaged samples could be decreased from the current 30 μm to 15–20 μm. This is possible because the overall picture can be gained from a multiscale approach[59] using synchrotron phase-contrast μCT. The 4D nanoimaging investigations can focus on the values/descriptors gathered in Box 2, and μCT, with a much larger FoV, will obtain overall details. On the other hand, the CNR/CR could be relaxed, for instance with slightly poorer SNR, and advanced denoising approaches could be implemented to counterbalance that. It is worth mentioning that we have employed so far nf-PXCT. However, holographic X-ray nanocomputed tomography (HXnCT),[60,61] could be equally adequate to reach the target time resolution. A HXnCT beamtime has been already awarded and the results will be reported elsewhere.

5.2. 4D Nanoimaging of Cement Hydration with Accelerating and Retarding Admixtures

When the aforementioned requirements are met, the doors are open to the study of scientifically interesting and technologically important challenges. For instance, the mechanism(s) of accelerating admixtures are not well understood.[51,62] This is the case even for $CaCl_2$, which has been employed in concretes for more than a century. There are indications that it could yield a more permeable C–S–H gel that permits faster ion diffusion, but it also modifies calcium supersaturation with respect to C–S–H gel and CH.[63] The comparison of the results for the *in situ* nanoimaging studies of cement hydration, in the absence and presence of admixture(s), may allow a mechanistic understanding and, therefore, a sound optimization of the processes. So far, the accelerators are being developed through an empirical approach, i.e. mainly trial an error. An accurate measurement of the scientific descriptors given in Box 2 is expected to improve

https://doi.org/10.1021/accountsmr.5c00018
Acc. Mater. Res. 2025, 6, 814–827

our understanding of early age cement hydration and the possible synergies between different (already known) accelerator admixtures like C−S−H nucleation seeding and alkanolamine addition.[51]

6. CONCLUSIONS

4D synchrotron hard X-ray nanoimaging of cement hydration is an emerging field. It is technically demanding, but synchrotron beamline teams are starting to deploy these techniques to nonexpert research groups. To make an impact, relevant conditions must be kept at the center of the research plan. Technical improvements are required in order to study the key acceleration/deceleration transition as previously discussed. If these requirements are met, the role of admixtures could be mechanistically understood. One key goal is to rationally accelerate cement hydration further, to be able to generally adopt low-carbon cements.

We should be able to develop better curing approaches where the sound understanding of cement hydration will allow the choice of the right combination of chemicals and experimental conditions that yield the target performances in a cost-effective manner: lowest possible CO_2 footprint, good flowability after mixing, and best possible mechanical strengths and durability.

AUTHOR INFORMATION

Corresponding Author

Miguel A.G. Aranda − *Departamento de Química Inorgánica, Cristalografía y Mineralogía, Universidad de Málaga, 29071 Málaga, Spain; Instituto Universitario de Materiales y Nanotecnología, IMANA, University of Malaga, 29071 Malaga, Spain;* orcid.org/0000-0001-7708-3578; Email: g_aranda@uma.es

Complete contact information is available at: https://pubs.acs.org/10.1021/accountsmr.5c00018

Funding

This project has received funding from the European Research Council (ERC-AdG) under the European Union's Horizon Europe research and innovation program [grant agreement No. 101139298, "Imaging the hydration of low-carbon CEMents with SYNchrotron X-rays (syn4cem)]", 2025/01−2029/12. Partial funding from PID2020−114650RB-I00 grant (Agencia Estatal de Investigación, Spain) cofunded by ERDF, is also acknowledged.

Notes

The author declares no competing financial interest.

Biography

Miguel A. G. Aranda is Professor of Inorganic Chemistry at the University of Malaga. He has been scientific director of ALBA synchrotron (2013-2019) and Chairman of the ESRF council (2018-2020). He is coeditor of the Journal of Synchrotron Radiation and he was Chair of the Commission on Synchrotron and XFEL Radiation of the IUCr (2021-2023). His main research interests are to contribute to reducing the CO_2 footprint of cements and improving circular economy through the use of byproducts in the building industry. He is actively investigating smectitic and kaolinitic Limestone Calcined Clay Cements as well as other SCMs such as natural pozzolans. The primary focus is the mechanistic understanding of cement hydration at early age by means of relevant fast 4D synchrotron X-ray nanoimaging in order to boost compressive strengths within at 1 day without performance degradation at later ages. To this end, it has recently obtained an ERC-AdG, acronym: syn4cem. More details at: https://sites.google.com/view/miguel-ag-aranda/.

ACKNOWLEDGMENTS

This is a team's effort, and therefore, I thank all the members of the cement research group at the University of Malaga and the external collaborators. Special thanks are due to Dr. Shiva Shirani and Mr. Alejandro Morales-Cantero for their help in the preparation of some figures. Access to synchrotron X-ray imaging beamlines, especially to cSAXS and TOMCAT BLs of SLS-PSI (Switzerland) and ID19 and ID16 BLs of ESRF (The European Synchrotron at Grenoble), is acknowledged. Finally, very fruitful and comprehensive discussions with Dr. Ana Diaz (senior scientist of PSI, Switzerland) on many technical details of synchrotron X-ray micro- and nanoimaging are gratefully acknowledged.

ABBREVIATIONS

AFt, $Ca_6Al_2(SO_4)_3(OH)_{12}\cdot 26H_2O$
BCDI, Bragg coherent diffraction imaging
C_2S, Ca_2SiO_4 or belite
C_3A, $Ca_3Al_2O_6$
C_3S, Ca_3SiO_5 or alite
C_4AF, $Ca_4Al_2Fe_2O_{10}$ or ferrite
CDI, coherent diffraction imaging
CH, $Ca(OH)_2$
CR, contrast resolution
CT, computed tomography
C-(A)−S-H gel, amorphous $\approx(CaO)_{1.5}(Al_2O_3)_{0.1}SiO_2(H_2O)_{4.0}$
C−S−H gel, amorphous $\approx(CaO)_{1.8}SiO_2(H_2O)_{4.0}$
FCDI, forward coherent diffraction imaging
Fe−Si-hg, amorphous $\approx Ca_3Fe_2(SiO_4)_{0.84}(OH)_{8.64}$
FIB-TEM, focused ion beam - transmission electron microscopy
ff-PXnCT, far-field ptychographic X-ray nanocomputed tomography
FoV, Field of View
Hc, $Ca_4Al_2(OH)_{13}(CO_3)_{0.5}(H_2O)_{5.5}$
HXnCT, holographic X-ray nanocomputed tomography
HXμCT, holographic X-ray microcomputed tomography
ITZ, interfacial transition zone
μCT, microcomputed tomography
nCT, nanocomputed tomography
nf-PXnCT, near-field ptychographic X-ray nanocomputed tomography
PC, Portland cement
PCE, polycarboxylate ether
ph-μCT, phase-contrast microcomputed tomography
ph-nCT, phase-contrast nanocomputed tomography
PSF, point spread function
PXnCT, ptychographic X-ray nanocomputed tomography
PXμCT, ptychographic X-ray microcomputed tomography
RVE, representative volume element
SCMs, supplementary cementitious materials
SEM, scanning electron microscopy
STEM, scanning transmission electron microscopy
TEM, transmission electron microscopy
SNR, signal-to-noise ratio
CNR, contrast to noise ratio
w/b, water to binder mass ratio

https://doi.org/10.1021/accountsmr.5c00018
Acc. Mater. Res. 2025, 6, 814−827

w/c, water to cement mass ratio

REFERENCES

(1) Taylor, H. F. W. *Cement Chemistry*, 2nd ed.; Thomas Telford Publishing, 1997.
(2) *Annual CO_2 emissions from cement*. https://ourworldindata.org/grapher/annual-co2-cement.
(3) *Cement Industry Energy and CO2 Performance Getting the Numbers Right (GNR)*. World Business Council for Sustainable Devlopment. 2016.
(4) Miller, S. A.; John, V. M.; Pacca, S. A.; Horvath, A. Carbon Dioxide Reduction Potential in the Global Cement Industry by 2050. *Cem. Concr. Res.* **2018**, *114*, 115−124.
(5) UN Environment; Scrivener, K. L.; John, V. M.; Gartner, E. Eco-Efficient Cements: Potential, Economically Viable Solutions for a Low-CO2, Cement-Based Materials Industry. *Cem. Concr. Res.* **2018**, *114*, 2−26.
(6) Habert, G.; Miller, S. A.; John, V. M.; Provis, J. L.; Favier, A.; Horvath, A.; Scrivener, K. L. Environmental Impacts and Decarbonization Strategies in the Cement and Concrete Industries. *Nat. Rev. Earth Environ.* **2020**, *1* (11), 559−573.
(7) Snellings, R.; Suraneni, P.; Skibsted, J. Future and Emerging Supplementary Cementitious Materials. *Cem. Concr. Res.* **2023**, *171*, No. 107199.
(8) Ruiz-Agudo, C.; Cölfen, H. Exploring the Potential of Nonclassical Crystallization Pathways to Advance Cementitious Materials. *Chem. Rev.* **2024**, *124*, 7538−7618.
(9) Hewlett, P. C.; Liska, M. *Lea's Chemistry of Cement and Concrete*, 5th ed.; Elsevier, 2017.
(10) Scrivener, K. L.; Snellings, R.; Lothenbach, B. *A Practical Guide to Microstructural Analysis of Cementitious Materials*; CRC Press: Boca Raton, FL, 2017. DOI: 10.1201/b19074.
(11) Aranda, M. A. G. Recent Studies of Cements and Concretes by Synchrotron Radiation Crystallographic and Cognate Methods. *Crystallogr. Rev.* **2016**, *22* (3), 150−196.
(12) Zhang, Z.; Yan, Y.; Geng, G. A Review of Micro-Resolved Crystochemical and Mechanical Probes for Sustainable Cement-Based Material Studies. *npj Mater. Sustain.* **2025**, *3*, 1.
(13) Scrivener, K. L.; Crumbie, A. K.; Laugesen, P. The Interfacial Transition Zone (ITZ) between Cement Paste and Aggregate in Concrete. *Interface Sci.* **2004**, *12* (4), 411−421.
(14) Georget, F.; Sui, S.; Wilson, W.; Scrivener, K. L. Reconciliation of Pore Structure Characterization Methods: The Simple Case of PC-Limestone Cement Pastes. *Cem. Concr. Res.* **2024**, *184*, No. 107624.
(15) Zhang, L.; Lüttge, A. Morphological Evolution of Dissolving Feldspar Particles with Anisotropic Surface Kinetics and Implications for Dissolution Rate Normalization and Grain Size Dependence: A Kinetic Modeling Study. *Geochim. Cosmochim. Acta* **2009**, *73* (22), 6757−6770.
(16) Yan, Y.; Geng, G. Does Nano Basic Building-Block of C-S-H Exist? − A Review of Direct Morphological Observations. *Mater. Des.* **2024**, *238*, No. 112699.
(17) Scrivener, K. L.; Ouzia, A.; Juilland, P.; Kunhi Mohamed, A. Advances in Understanding Cement Hydration Mechanisms. *Cem. Concr. Res.* **2019**, *124*, No. 105823.
(18) Juilland, P.; Gallucci, E.; Flatt, R.; Scrivener, K. L. Dissolution Theory Applied to the Induction Period in Alite Hydration. *Cem. Concr. Res.* **2010**, *40* (6), 831−844.
(19) Ouzia, A.; Scrivener, K. L. The Needle Model: A New Model for the Main Hydration Peak of Alite. *Cem. Concr. Res.* **2019**, *115*, 339−360.
(20) Neubauer, J.; Sowoidnich, T.; Valentini, L.; Schulbert, C.; Naber, C.; Rößler, C.; DaSilva, J.; Bellmann, F. Evolution of the Particle Size Distribution of Tricalcium Silicate during Hydration by Synchrotron X-Ray Nano-Tomography. *Cem. Concr. Res.* **2022**, *156*, No. 106769.
(21) Masoero, E.; Thomas, J. J.; Jennings, H. M. A Reaction Zone Hypothesis for the Effects of Particle Size and Water-to-Cement Ratio on the Early Hydration Kinetics of C3S. *J. Am. Ceram. Soc.* **2014**, *97* (3), 967−975.
(22) Honorio, T.; Bary, B.; Benboudjema, F.; Poyet, S. Modeling Hydration Kinetics Based on Boundary Nucleation and Space-Filling Growth in a Fixed Confined Zone. *Cem. Concr. Res.* **2016**, *83*, 31−44.
(23) Shen, D.; Wang, X.; Wu, S. Determining Hydration Mechanisms for Initial Fall and Main Hydration Peak in Tricalcium Silicate Hydration Using a Two-Scale Hydration Simulation Model. *Cem. Concr. Res.* **2022**, *156* (1), No. 106763.
(24) Cuesta, A.; Zea-Garcia, J. D.; Londono-Zuluaga, D.; De la Torre, A. G.; Santacruz, I.; Vallcorba, O.; Dapiaggi, M.; Sanfélix, S. G.; Aranda, M. A. G. Multiscale Understanding of Tricalcium Silicate Hydration Reactions. *Sci. Rep.* **2018**, *8* (1), 8544.
(25) Allen, A. J.; Thomas, J. J.; Jennings, H. M. Composition and Density of Nanoscale Calcium−Silicate−Hydrate in Cement. *Nat. Mater.* **2007**, *6* (4), 311−316.
(26) Juilland, P.; Nicoleau, L.; Arvidson, R. S.; Gallucci, E. Advances in Dissolution Understanding and Their Implications for Cement Hydration. *RILEM Technol. Lett.* **2017**, *2*, 90−98.
(27) Gallucci, E.; Mathur, P.; Scrivener, K. Microstructural Development of Early Age Hydration Shells around Cement Grains. *Cem. Concr. Res.* **2010**, *40* (1), 4−13.
(28) de Matos, P. R.; Andrade Neto, J.; Jansen, D.; De la Torre, A. G.; Kirchheim, A. P.; Campos, C. E. M. In-Situ Laboratory X-Ray Diffraction Applied to Assess Cement Hydration. *Cem. Concr. Res.* **2022**, *162*, No. 106988.
(29) Dong, P.; Allahverdi, A.; Andrei, C. M.; Bassim, N. D. Liquid Cell Transmission Electron Microscopy Reveals C-S-H Growth Mechanism during Portland Cement Hydration. *Materialia* **2022**, *22*, No. 101387.
(30) Withers, P. J.; Bouman, C.; Carmignato, S.; Cnudde, V.; Grimaldi, D.; Hagen, C. K.; Maire, E.; Manley, M.; Du Plessis, A.; Stock, S. R. X-Ray Computed Tomography. *Nat. Rev. Methods Prim.* **2021**, *1*, 18.
(31) Monteiro, P. J. M.; Geng, G.; Marchon, D.; Li, J.; Alapati, P.; Kurtis, K. E.; Qomi, M. J. A. Advances in Characterizing and Understanding the Microstructure of Cementitious Materials. *Cem. Concr. Res.* **2019**, *124*, No. 105806.
(32) Qoku, E.; Xu, K.; Li, J.; Monteiro, P. J. M.; Kurtis, K. E. Advances in Imaging, Scattering, Spectroscopy, and Machine Learning-Aided Approaches for Multiscale Characterization of Cementitious Systems. *Cem. Concr. Res.* **2023**, *174*, 107335.
(33) du Plessis, A.; Boshoff, W. P. A Review of X-Ray Computed Tomography of Concrete and Asphalt Construction Materials. *Constr. Build. Mater.* **2019**, *199*, 637−651.
(34) Brisard, S.; Serdar, M.; Monteiro, P. J. M. Multiscale X-Ray Tomography of Cementitious Materials: A Review. *Cem. Concr. Res.* **2020**, *128*, No. 105824.
(35) Kong, W.; Wei, Y.; Wang, S.; Chen, J.; Wang, Y. Research Progress on Cement-Based Materials by X-Ray Computed Tomography. *Int. J. Pavement Res. Technol.* **2020**, *13* (4), 366−375.
(36) Sugiyama, T.; Promentilla, M. A. B. Advancing Concrete Durability Research through X-Ray Computed Tomography. *J. Adv. Concr. Technol.* **2021**, *19*, 730−755.
(37) Chung, S. Y.; Kim, J. S.; Stephan, D.; Han, T.-S. Overview of the Use of Micro-Computed Tomography (Micro-CT) to Investigate the Relation between the Material Characteristics and Properties of Cement-Based Materials. *Constr. Build. Mater.* **2019**, *229*, No. 116843.
(38) Willmott, P. *An Introduction to Synchrotron Radiation: Techniques and Applications*; Wiley, 2011.
(39) Quenot, L.; Bohic, S.; Brun, E. X-Ray Phase Contrast Imaging from Synchrotron to Conventional Sources: A Review of the Existing Techniques for Biological Applications. *Appl. Sci. 2022, Vol. 12, Page 9539* **2022**, *12*, 9539.
(40) Pfeiffer, F. X-Ray Ptychography. *Nat. Photonics* **2018**, *12* (1), 9−17.
(41) Guizar-Sicairos, M.; Thibault, P. Ptychography: A Solution to the Phase Problem. *Phys. Today* **2021**, *74* (9), 42.
(42) Donnelly, C.; Finizio, S.; Gliga, S.; Holler, M.; Hrabec, A.; Odstrčil, M.; Mayr, S.; Scagnoli, V.; Heyderman, L. J.; Guizar-Sicairos, M.; Raabe, J. Time-Resolved Imaging of Three-Dimensional Nanoscale Magnetization Dynamics. *Nat. Nanotechnol.* **2020**, *15*, 356−360.

https://doi.org/10.1021/accountsmr.5c00018
Acc. Mater. Res. 2025, 6, 814−827

(43) van Heel, M.; Schatz, M. Fourier Shell Correlation Threshold Criteria. *J. Struct. Biol.* **2005**, *151* (3), 250−262.
(44) ISO. *Microbeam analysis — Scanning electron microscopy — Methods of evaluating image sharpness*; ISO/TS 24597:2011; https://www.iso.org/es/contents/data/standard/05/57/55760.html (accessed 2025−03−26).
(45) Li, X.; Hu, Q.; Robertson, B.; Ley, M. T.; De Andrade, V. J.; Sokhansefat, G. Direct Observation of C3S Particle Dissolution Using Fast Nano X-Ray Computed Tomography. *Cem. Concr. Res.* **2023**, *166*, No. 107097.
(46) Shirani, S.; Cuesta, A.; Morales-Cantero, A.; Santacruz, I.; Diaz, A.; Trtik, P.; Holler, M.; Rack, A.; Lukic, B.; Brun, E.; Salcedo, I. R.; Aranda, M. A. G. 4D Nanoimaging of Early Age Cement Hydration. *Nat. Commun.* **2023**, *14*, 2652.
(47) Vanpeene, V.; Villanova, J.; Suuronen, J. P.; King, A.; Bonnin, A.; Adrien, J.; Maire, E.; Roué, L. Monitoring the Morphological Changes of Si-Based Electrodes by X-Ray Computed Tomography: A 4D-Multiscale Approach. *Nano Energy* **2020**, *74*, No. 104848.
(48) Oey, T.; Kumar, A.; Bullard, J. W.; Neithalath, N.; Sant, G. The Filler Effect: The Influence of Filler Content and Surface Area on Cementitious Reaction Rates. *J. Am. Ceram. Soc.* **2013**, *96* (6), 1978−1990.
(49) Zunino, F.; Scrivener, K. L. The Influence of the Filler Effect on the Sulfate Requirement of Blended Cements. *Cem. Concr. Res.* **2019**, *126*, No. 105918.
(50) Morales-Cantero, A.; Cuesta, A.; De la Torre, A. G.; Santacruz, I.; Mazanec, O.; Borralleras, P.; Weldert, K. S.; Gastaldi, D.; Canonico, F.; Aranda, M. A. G. C-S-H Seeding Activation of Portland and Belite Cements: An Enlightening in Situ Synchrotron Powder Diffraction Study. *Cem. Concr. Res.* **2022**, *161*, No. 106946.
(51) Cuesta, A.; Morales-Cantero, A.; De la Torre, A. G.; Aranda, M. A. G. Recent Advances in C-S-H Nucleation Seeding for Improving Cement Performances. *Materials (Basel).* **2023**, *16*, 1462.
(52) Morales-Cantero, A.; De la Torre, A. G.; Cuesta, A.; Santacruz, I.; Bernal, I. M.R.; Mazanec, O.; Dalla-Libera, A.; Borralleras, P.; Aranda, M. A.G. In Situ Synchrotron Powder Diffraction Study of LC3 Cement Activation at Very Early Ages by C-S-H Nucleation Seeding. *Cem. Concr. Res.* **2024**, *178*, No. 107463.
(53) Vigor, J. E.; Bernal, S. A.; Xiao, X.; Provis, J. L. Time-Resolved 3D Characterisation of Early-Age Microstructural Development of Portland Cement. *J. Mater. Sci.* **2022**, *57* (8), 4952−4969.
(54) Seiller, J.; Bonnal, T.; Adrien, J.; Meille, S.; Tadier, S.; Maire, E.; Bonnin, A. 4D in Situ Monitoring of the Setting of α Plaster Using Synchrotron X-Ray Tomography with High Spatial and Temporal Resolution. *Constr. Build. Mater.* **2021**, *304*, No. 124632.
(55) Geng, G.; Myers, R. J.; Yu, Y.-S.; Shapiro, D. A.; Winarski, R.; Levitz, P. E.; Kilcoyne, D. A. L.; Monteiro, P. J. M. Synchrotron X-Ray Nanotomographic and Spectromicroscopic Study of the Tricalcium Aluminate Hydration in the Presence of Gypsum. *Cem. Concr. Res.* **2018**, *111*, 130−137.
(56) Cuesta, A.; De la Torre, A. G.; Santacruz, I.; Trtik, P.; Da Silva, J. C.; Diaz, A.; Holler, M.; Aranda, M. A. G. In Situ Hydration Imaging Study of a Ye'elimite Paste by Ptychographic X-Ray Computed Tomography. *39th International Conference on Cement Microscopy, ICMA 2017* **2017**, 17−32.
(57) Shirani, S.; Cuesta, A.; Santacruz, I.; De la Torre, A. G.; Diaz, A.; Trtik, P.; Holler, M.; Aranda, M. A. G. X-Ray near-Field Ptychographic Nanoimaging of Cement Pastes. *Cem. Concr. Res.* **2024**, *185*, No. 107622.
(58) Cuesta, A.; De la Torre, A. G.; Santacruz, I.; Diaz, A.; Trtik, P.; Holler, M.; Lothenbach, B.; Aranda, M. A. G. Quantitative Disentanglement of Nanocrystalline Phases in Cement Pastes by Synchrotron Ptychographic X-Ray Tomography. *IUCrJ.* **2019**, *6* (3), 473−491.
(59) Bonnin, A.; Lovric, G.; Marone, F.; Olbinado, M.; Schlepütz, C. M.; Stampanoni, M. Multiscale Synchrotron Propagation-Based Phase-Contrast X-Ray Tomographic Microscopy at the TOMCAT Beamline: Latest Achievements and Future Plans. *Synchrotron Radiat. News* **2024**, *37*, 4−9.
(60) Du, M.; Gürsoy, D.; Jacobsen, C. Near, Far, Wherever You Are: Simulations on the Dose Efficiency of Holographic and Ptychographic Coherent Imaging. *J. Appl. Crystallogr.* **2020**, *53* (3), 748−759.
(61) Monaco, F.; Hubert, M.; Da Silva, J. C.; Favre-Nicolin, V.; Montinaro, D.; Cloetens, P.; Laurencin, J. A Comparison between Holographic and Near-Field Ptychographic X-Ray Tomography for Solid Oxide Cell Materials. *Mater. Charact.* **2022**, *187*, No. 111834.
(62) Dorn, T.; Blask, O.; Stephan, D. Acceleration of Cement Hydration − A Review of the Working Mechanisms, Effects on Setting Time, and Compressive Strength Development of Accelerating Admixtures. *Constr. Build. Mater.* **2022**, *323*, No. 126554.
(63) Bentz, D. P.; Zunino, F.; Lootens, D. Chemical vs. Physical Acceleration of Cement Hydration. *Concr. Int.* **2016**, *38* (11), 37−44.

https://doi.org/10.1021/accountsmr.5c00018
Acc. Mater. Res. 2025, 6, 814−827